IMMI: the role of well calibration in the context of high geological complexity

Sergio Romahn and Kris Innanen

ABSTRACT

Iterative modelling, migration and inversion (IMMI) aims to incorporate standard processing techniques into the process of full waveform inversion (FWI). IMMI proposes the use of any depth migration method to obtain the gradient, while FWI uses a two-way wave migration, commonly reverse time migration (RTM). IMMI uses well calibration to scale the gradient, instead of applying a line search to find the scalar or an approximation of the inverse Hessian matrix. We used a phase shift plus interpolation (PSPI) migration with a deconvolution imaging condition that works as a gain correction. We show the suitability of estimating the subsurface velocity model by applying IMMI's approach using synthetic examples with increasingly geological complexity. We found consistently low errors in the well calibration location, even in the most complex settings. This suggests that the gradient obtained by applying PSPI migration points to the correct direction to minimize the objective function, and that well calibration provides an optimal scale. This is promising in the context of reservoir characterization, where we may have many control wells. We found that IMMI satisfactorily performs in the presence of moderate lateral velocity changes. The results, for the scenario of strong lateral velocity changes, indicate that well calibration is a worthy option providing that the well is representative of the geology in the zone of interest.

INTRODUCTION

Lailly (1983) and Tarantola (1984) provided the mathematical basis for full waveform seismic inversion. They showed that FWI and migration are strongly linked, in what Margrave et al. (2010) call the fundamental theorem of FWI, which is summarized in Equation 1.

$$\delta v(x,z) = \lambda \nabla_v \phi_k(x,z,w) = \lambda \int \sum_{s,r} \omega^2 \hat{\Psi}_s(x,z,\omega) \delta \hat{\Psi}^*_{r(s),k}(x,z,\omega) d\omega \qquad (1)$$

Where $\delta v(x,z)$ is the velocity update, λ is a scalar constant, ∇_v is the gradient with respect to the velocity model v, $\phi_k(x,z,w)$ is the objective function, w is angular frequency, $\hat{\Psi}_s(x,z,\omega)$ is a model of the source wavefield for source s propagated to all (x,z), $\delta \hat{\Psi}^*_{r(s),k}(x,z,\omega)d\omega$ is the kth data residual for source s back propagated to all (x,z), $*$ means complex conjugation. The residual $\delta \hat{\Psi}^*_{r(s),k}(x,z,\omega)$ is the difference between the observed data Ψ_r and the modeled data $\Psi_{r,k}$.

The objective function measures the difference between the recorded data Φ and the modelled data Φ_k at the kth iteration (Equation 2).

$$\phi_k = \sum_{s,r} (\Psi - \Psi_k)^2 \qquad (2)$$

Equation 1 says that the gradient of the objective function ($\nabla_v \phi_k$) is formed by correlating the time inverse residuals propagated into the medium with the source field propagated into the medium. This the core of FWI. The gradient is the element that contains the direction of the velocity update in the minimization scheme. The other element is the inverse Hessian or an approximation of it. If the inverse Hessian is replaced by a scalar λ, the mathematical effort is reduced to the gradient or steepest-descent method. λ scales the gradient to be converted into a velocity perturbation. λ is commonly estimated by a line-search method which requires an extra forward problem per shot (Virieux and Operto, 2009).

Margrave et al. (2010) described the process of FWI as an iterative cycle that involves four main steps shown in figure 1.
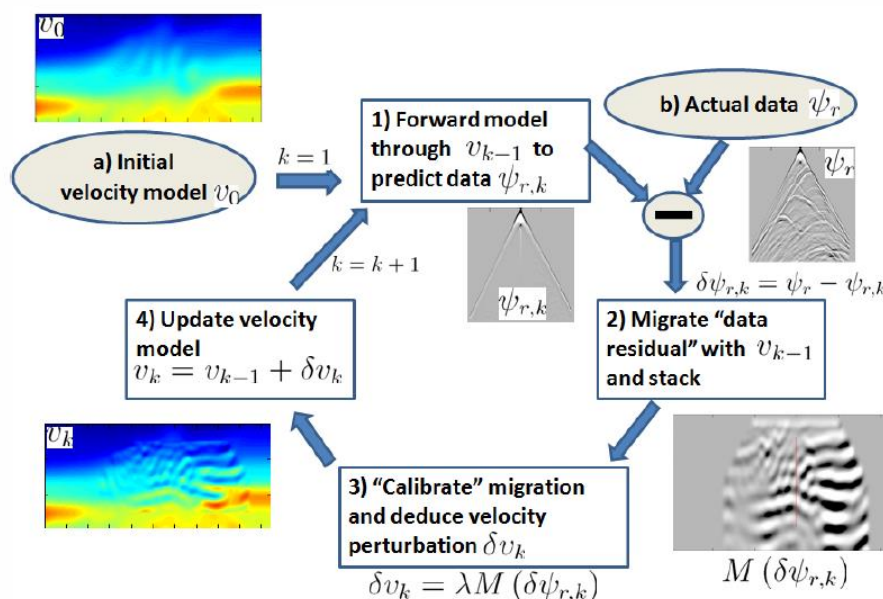

FIG. 1. The cycle of FWI (Margrave et al., 2010)

.

The four steps of the FWI's cycle are:

1) Generating synthetic seismic data (predicted data $\Psi_{r,k}$) from a very smoothed initial model v_o, and calculation of the data residual $\delta\Psi_{r,k} = \Psi_r - \Psi_{r,k}$.

2) Pre-stack depth migration using the current velocity model ($v_{k-1} = v_o$, for iteration 1) of the data residual and stack $M(\delta\Psi_{r,k})$. This provides the gradient or update direction.

3) Scaling or calibrating the gradient that produces the velocity perturbation δv_k.

4) Updating current velocity model $v_k = v_{k-1} + \delta v_k$, which will be used in the next iteration.

IMMI, introduced by Margrave et al. (2012), was thought as an alternative for accomplishing FWI by using tools already available and widely used by the industry. Examples of IMMI's philosophy are the application of any depth migration method and the incorporation of well information for scaling the gradient. Furthermore; the authors suggest that using a deconvolution imaging condition, instead of the correlation used in RTM, may achieve something very similar to the role of the main diagonal elements of the inverse Hessian, which is a gain correction as illustrated by Shin et al. (2001). Pan et al. (2014) applied the IMMI method, compared the crosscorrelation and deconvolution imaging conditions, and showed that using a deconvolution based gradient can compensate the geometrical spreading.

Following IMMI's approach, we use the phase shift plus interpolation migration method (one-way wave migration) with a deconvolution imaging condition to obtain the gradient. PSPI, presented by Gazdag and Sguazzero (1984), allows selecting a range of frequencies of interest which is very convenient to explore frequency employment strategies in FWI. Pratt (1999) suggested that starting the inversion using low frequencies and then moving to higher frequencies may help to avoid local minima. We will follow this strategy.

The scale λ in Equation 1, is estimated in the form of a match filter that equates the size of the gradient to the size of the velocity residual in a well location. The velocity residual is the difference between the well velocity and the current velocity model. We will present more details of this process in the next section.

WELL CALIBRATION VS GEOLOGICAL COMPLEXITY

We will evaluate the performance of the well calibration technique in three different geological models (figure 2). The first model is constituted by horizontal layers with a low velocity stratigraphic target at a depth of 2500 m. The second one is a modification of the Marmousi model where the normal faults were substituted by folded layers. This modification produces moderate lateral velocity changes above the geological target. The target is an anticline that works as a trap of a low velocity hydrocarbon zone. The complete Marmousi model was used for the third case. Normal faults above the target produce strong lateral velocity changes. The depth, size and velocity contrast of the target is the same for the three models. Two wells are displayed in each model (figure 2). Well C, outside the target, will be used for calibrating the gradient. Well B will be used to know the error in the target location.

Model 1: horizontal layers

We will show the process of IMMI for Model 1 in detail. All the steps described in this section will be applied to Model 2 and 3. All parameters (wavelet, seismic acquisition parameters, frequency range, mute, number of iterations, etc.) will be the same, so we are able to compare the results.
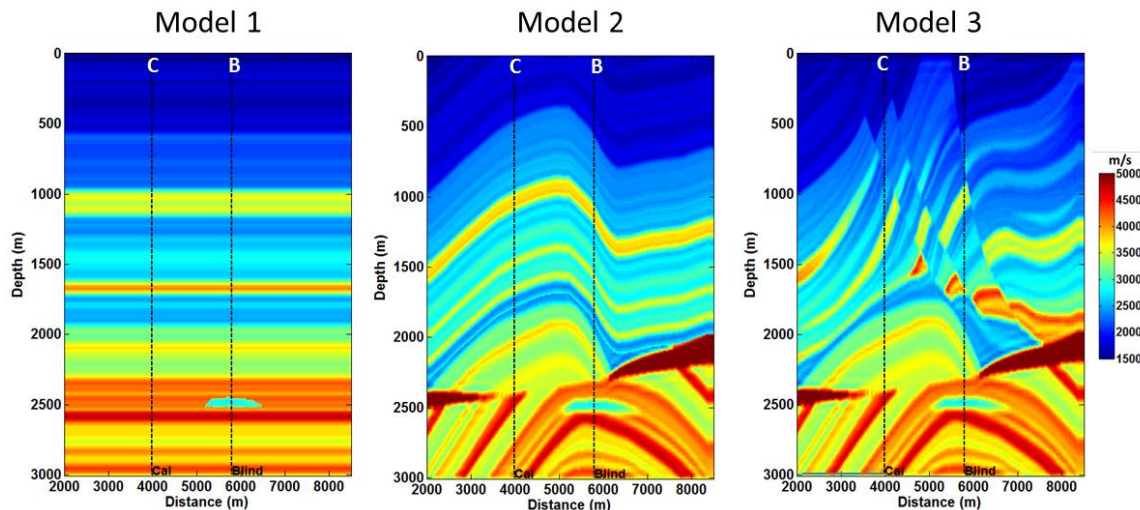
FIG. 2. Velocity models used to evaluate IMMI's performance in the context of high geological complexity.

Observed shots

The observed shots for this experiment are the idealized version of the ones that would be recorded on the field. We generated these shots by using an acoustic finite-difference algorithm to propagate the wavefield. A minimum phase wavelet with a dominant frequency of 20 Hz was used as seismic source.

We took into account the most complex model 3 to define the acquisition parameters. Full fold and migration zones were considered to properly record the target. The sources are placed every 50 m from 2100 to 9250 m, giving 144 shots in total. We located receiver stations along the whole model every 10 m, and all of them are kept alive for each shot. However, the maximum useful offset is approximately 5500 m, for a recorded time of 3 seconds. We considered maximum offsets of 3000 m to define the full fold zone, that will be at a distance of approximately 1500 meters from the first and last shots.

An example of a shot centered over the target is shown in figure 3. The velocity curve is also displayed. There are three prominent seismic events: two of them correspond to high velocity layers at 1.1 and 1.5 seconds, and the third event is related to the low velocity target around 2 seconds.

First iteration

The initial velocity model was generated by applying a Gaussian smoother of width 290 meters to the true velocity model (figure 4-A). Figure 4-B shows a comparison between the true and initial velocities at well B location. We compare the amplitude spectra of the initial and true velocities in figure 4-C. The reflectivity of the velocity (with constant density) was used to calculate the spectrum. The amplitude spectrum of the seismic is also plotted. We observe that the initial velocity model provides no more than 2 Hz of geological information. The true velocity model mainly contains information between 1 and 30 Hz,
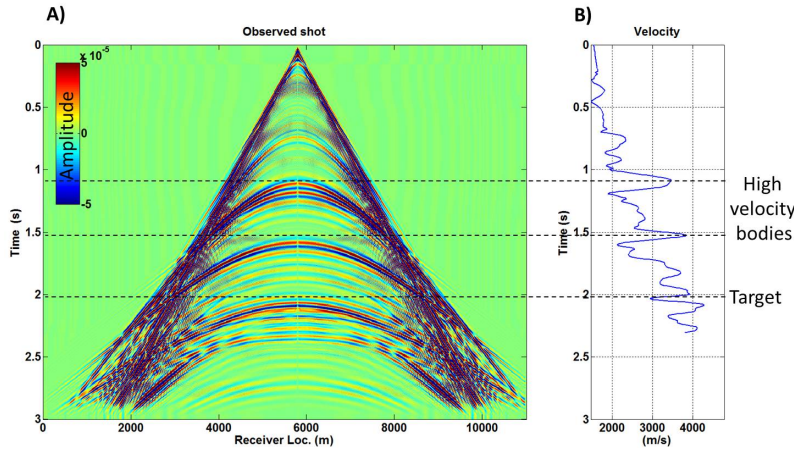
FIG. 3. A) Observed seismic shot above the geological target. B) Velocity curve in the shot location.

with the main events around 12 Hz. The seismic data has a dominant frequency of around 15 Hz and provides information between 7 and 25 Hz. There is gap between 2 and 5 Hz where neither the initial model nor the seismic data contribute.
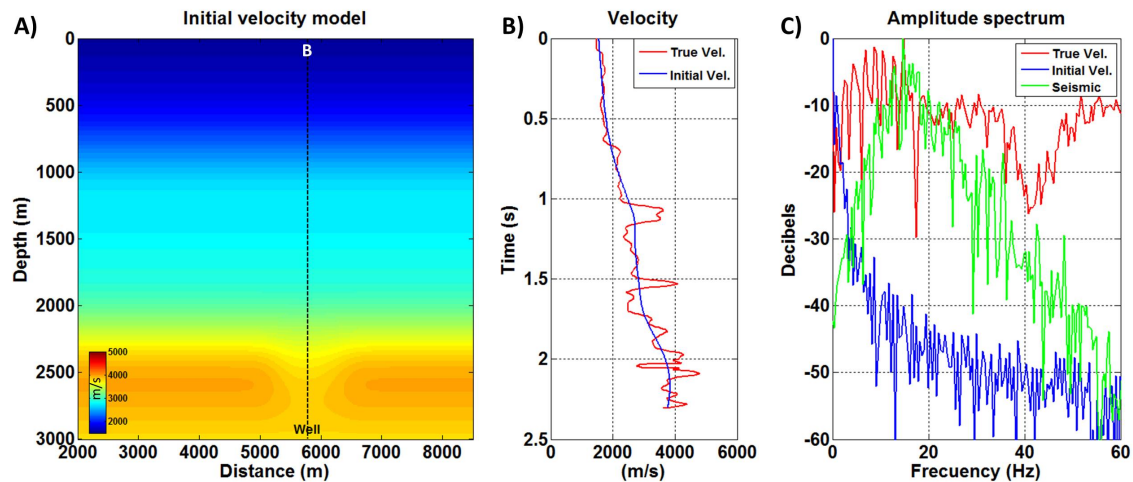

FIG. 4. A) Initial model for the first iteration in the inversion. B) Initial velocity vs true velocity. C) Amplitude spectra of the seismic, initial and true velocities.

Synthetic shots were generated by using the initial model, these shots are called the modelled ones (figure 5-B). The modelled shots for the first iteration do not have any important seismic reflection because there are no significant velocity contrasts in the initial model. The main event is the direct wave. The difference between the observed and the modelled shots is the data residual, which is, for this iteration, mainly the observed shot with a slightly modified direct wave (figure 5-C).

We obtain a data residual per shot, then they are migrated in depth by using the PSPI method, which allows introducing a specific frequency range. We used frequencies between 1 and 5 Hz for the first iteration. A mute, before stacking the residuals, is commonly applied to avoid migration artifacts (figure 6). We tested a narrow and a wide mute, and found that
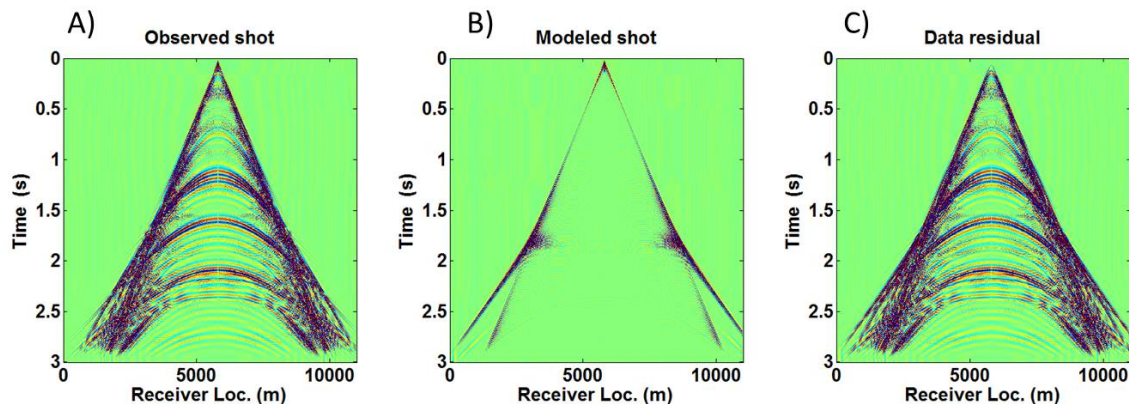
FIG. 5. A) Observed shot. B) Modelled shots for the iteration 1. C) Difference between observed and modelled shots for the first iteration.

the wide one produces the smallest error in the first iteration; however, the inverted velocity in the shallow part tends to be overestimated as we move to higher frequencies with this kind of mute. We changed to a narrow mute for the shallower part, and a wide mute for the deeper part from the second iteration, obtaining better results in the three geological scenarios.

The product of stacking the migrated data residuals is the gradient, which is shown in figure 7. The gradient has an order of magnitude of -5, and needs to be scaled in order to be converted into a velocity perturbation.
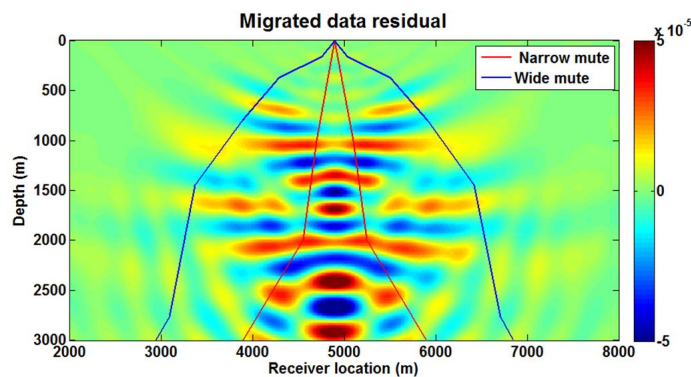
FIG. 6. Migrated data residual for the shot in figure 5. The frequency range is 1-5 Hz. The wide mute was used only for the first iteration, then we changed to the narrow mute.

The next step is to scale or calibrate the gradient. We use well C to perform this process. Note that well C is located outside the target as shown in figure 2. The well calibration technique was described by Margrave et al. (2010). We summarize this process below.

Firstly, the difference δvel, between the well and model velocities is calculated. The second step is to estimate the amplitude scalar a and a phase rotation ϕ that make the gradient trace g more like δvel. The scalar a is found such that $\delta vel - ag$ is minimized by least squares. Finally, a convolutional match filter is obtained with a and ϕ. This match filter is applied to every gradient traces to obtain the velocity update. Figure 8 shows this
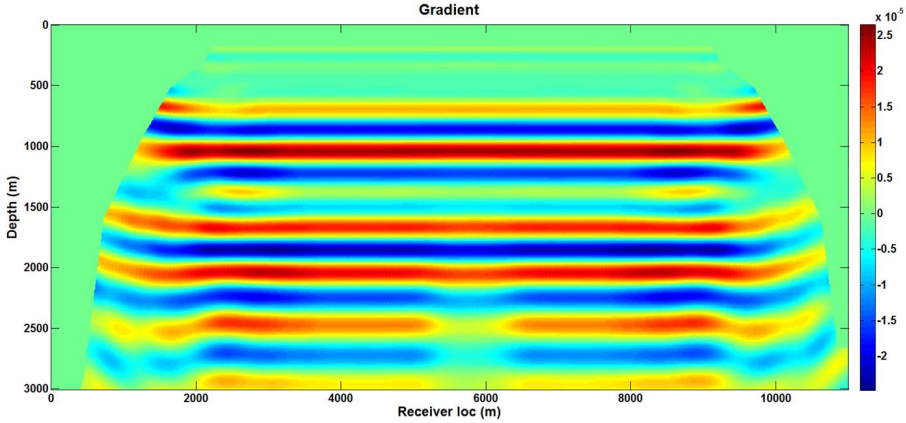
FIG. 7. The stack of all migrated data residuals produces the gradient.

process. Note that the gradient after being scaled has a magnitude order of 2, a now has become a suitable velocity update.
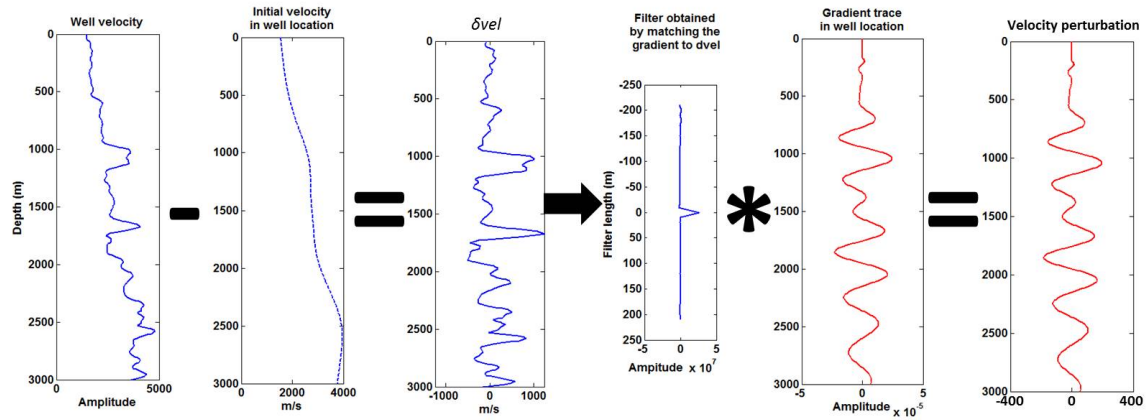

FIG. 8. Well calibration. The difference between true and initial velocities (δvel) is used to find a match filter that makes the gradient more like δvel. * means convolution.

A new velocity model, that will be used in the next iteration, is obtained by adding the velocity update to the current velocity model (figure 9).

More iterations

The inputs for the next iterations are the frequency range and the updated velocity model. Figure 10 shows how the frequency range was increased by 1 Hz each iteration. The average size of the velocity update, displayed on the right, tells how much those specific frequencies contribute to the construction of the model. The first frequency range from 1 to 5 Hz has an average size of 190 m/s, which represents the highest contribution to the model. The update size progressively decreases as we move to higher frequencies; however, they contribute to solve the fine details as we will see next.

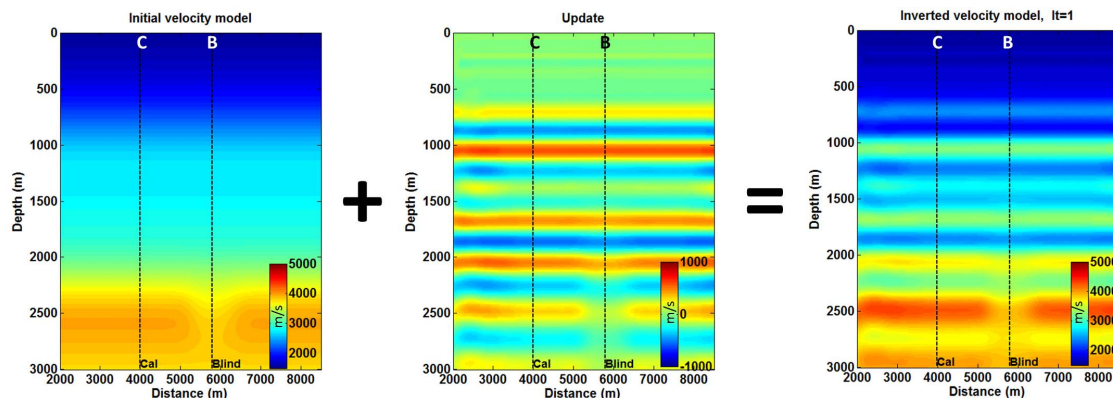Figure 11 shows the evolution of the inverted model from the initial velocity model

FIG. 9. The initial velocity model plus the velocity update produce a new model that will be used in the next iteration.
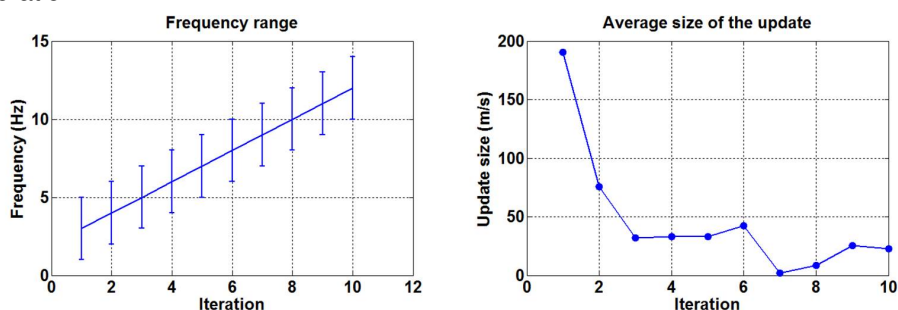

FIG. 10. Frequency range and update size for each iteration. The update size expresses the contribution of the respective frequency range to the model building.

to the 10th iteration at the calibration and blind well locations. We observe rapid changes in the first 2 iterations, then they steadily become smaller. The shallow part is mainly solved in the first 3 iterations, and the deep part is solved as we go to higher frequencies. Frequencies between 6 and 14 Hz, between iterations 6 and 10, contribute to recover the target in the blind well. The error, plotted at the right side, was calculated as the average of the absolute value of the difference between the inverted (V_i) and the well velocity (V_w), and was normalized respect to the error for the initial model. The blind well error is slightly greater than the error in the calibration well. The only difference between wells is the low velocity body in the blind well at 2500 m-depth. This observation rises the next question: Is well calibration valid in a context of high geological complexity? We will try to answer this question in the following section.

We stopped the inversion at the 10th iteration, because velocity artifacts in the shallow part become more prominent if we incorporate frequencies higher than 14 Hz (figure 12).

Figure 13 shows the comparison among the initial, inverted and true velocity models. The inversion is able to recover the most important features of the true model: the two high velocity layers at 1000 and 1750 m of depth, and the low velocity body at 2500 m of depth. The error in the model was calculated as the average error of all traces inside the full fold zone. The model error is similar to the error in the calibration well, as is expected from a model of horizontal layers. The amplitude spectra of the initial, true and inverted models
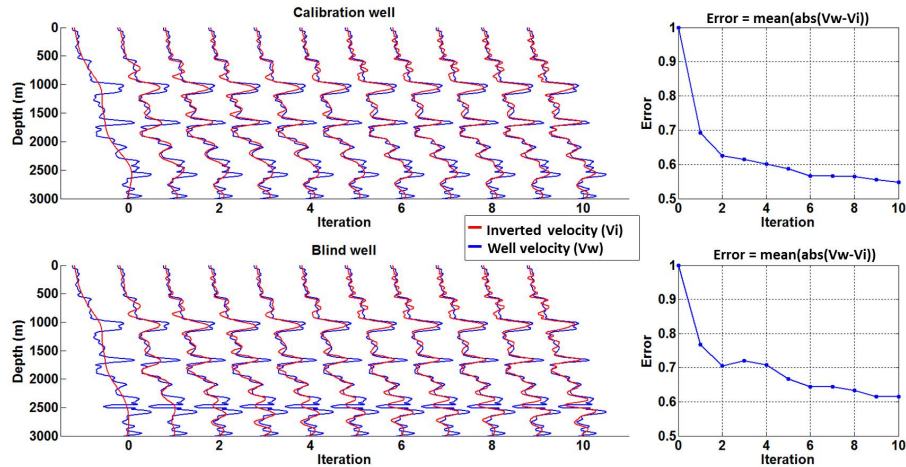
FIG. 11. Model 1: Inverted velocity evolution with iteration in calibration and blind wells. The error is the mean of the absolute value of the difference between inverted (V_i) and well velocities (V_w).
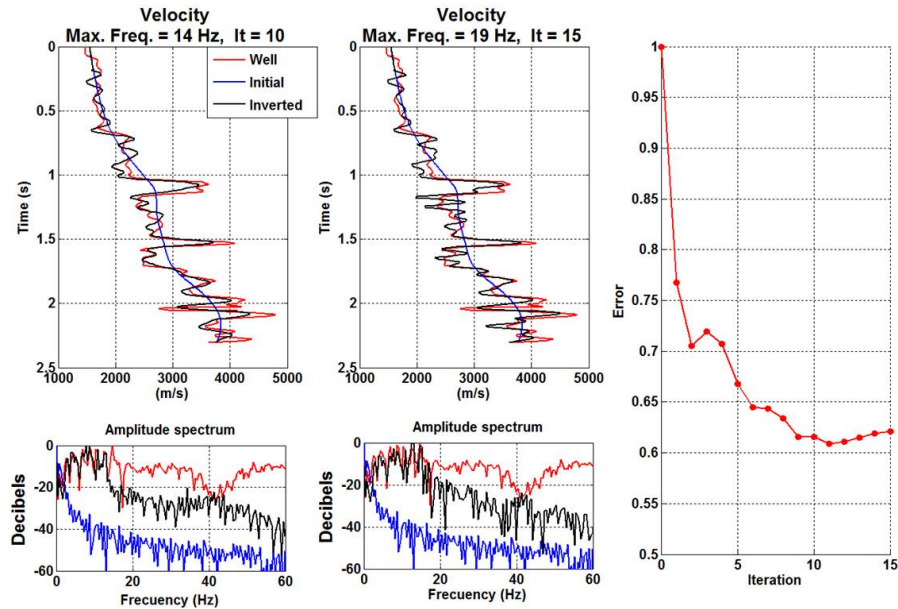

FIG. 12. Inverted velocity in blind well for the 10th and 15th iterations. High-frequency artifacts become prominent as we move to higher frequencies and the error increases.

are shown in the right corner of figure 13. We observe that the inversion is able to resemble the amplitude spectrum of the true model up to 14 Hz.

The spatial distribution of the error is shown in Figure 14. The average error of each trace is displayed above the section. This represents the horizontal error. We are only taking into account the full fold zone to evaluate the inversion. The error is slightly higher in the target zone than in areas where the velocity is similar to the calibration well C. We will compare the horizontal error for the three models in order to know how the error behaves when we have only one calibration well and the geological complexity increases.
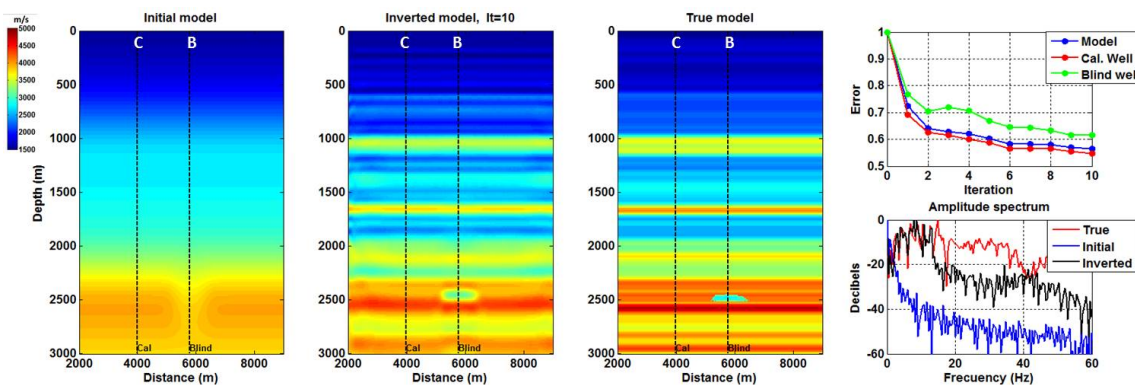
FIG. 13. Model 1: Comparison among initial, inverted and true velocity models. The error in the model was calculated as the average error of all traces inside the full fold zone.
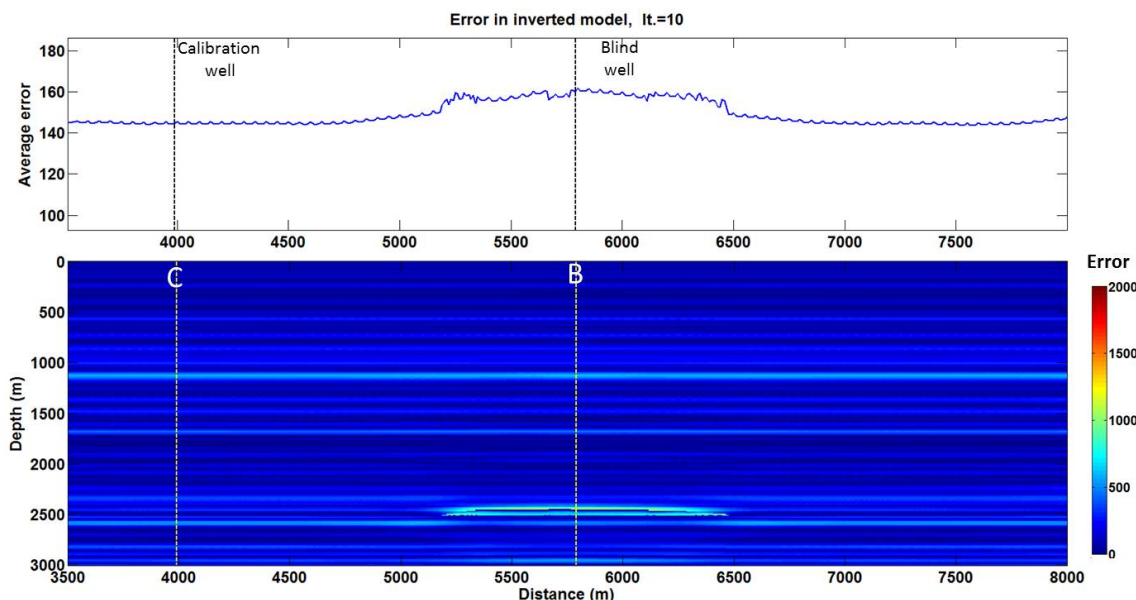

FIG. 14. Model 1: Spatial distribution of the error. The error in the section is the absolute value for the difference between true and inverted model. The average error per trace is displayed above the section.

Model 2: modified Marmousi model - moderate lateral velocity changes

Figure 15 shows the evolution of the inverted velocity from the initial model to iteration 10 in the calibration and blind wells. The normalized error with respect to the initial model is shown in the right side. The error steadily decreases from iteration 1 to 6 in both wells. It continues dropping from iteration 7 to 10 in a smaller rate, and subtle improvements are observed at the depth of 2500 m in the calibration well. Meanwhile, the error does not have a significant change from iteration 7 to 10 in the blind well. The error is consistently smaller in the calibration well than in the blind well.

Figure 16 shows the comparison among the initial, inverted and true models. The inversion is able to resolve all the main features of the true model: the velocity contrasts in the

folded layers from 0 to 2400 m, the high velocity bodies between 2000 and 2500 m, and the target at 2500 m of depth. We note that the right-side flank of the deeper anticline is blurred and undefined, which could be due to the shadow of the high velocity body above this zone and/or a deficient seismic coverage.
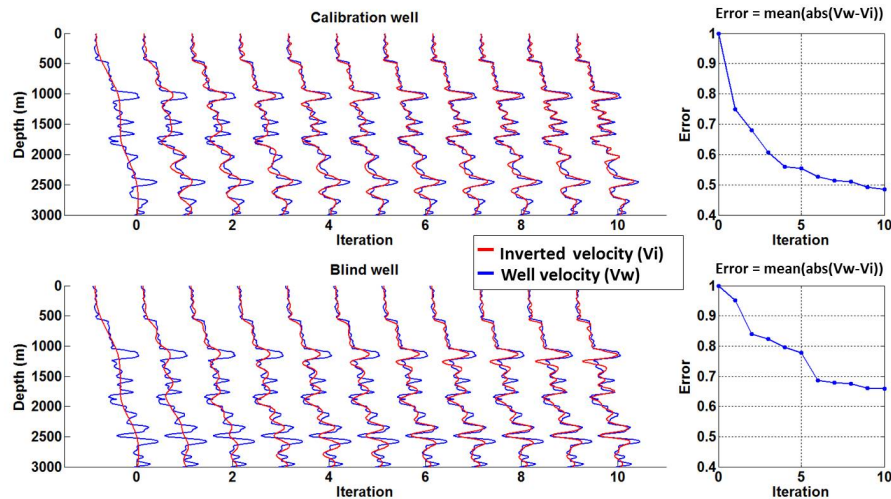

FIG. 15. Model 2: Inverted velocity evolution with iteration in calibration and blind wells.
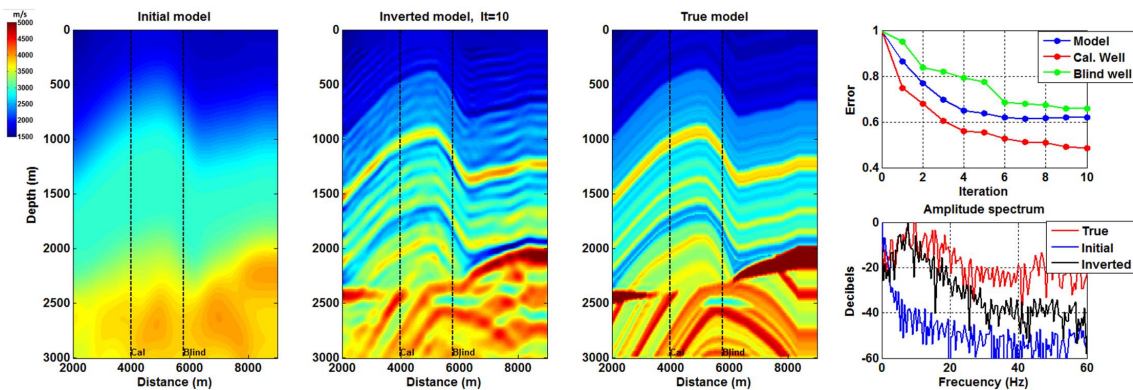

FIG. 16. Model 2: Comparison among initial, inverted and true velocity models.

The spatial distribution of the error is shown in Figure 17. The average error of each trace in the model is displayed above the section. The smallest errors occur around the calibration well. The highest error corresponds to the area where the high velocity body is located between 6200 and 8000 m in the horizontal axis.

Model 3: complete Marmousi model - strong lateral velocity changes

Figure 18 shows the inversion performance in the context of abrupt lateral velocity changes in Marmousi model. The inversion produces good results in the calibration well location, where the error consistently decreases with each iteration, specially from the first to the fifth. On the other hand, the inversion in the blind well location satisfactorily resolves the shallow part. However, the deeper part has been slightly underestimated, specially in
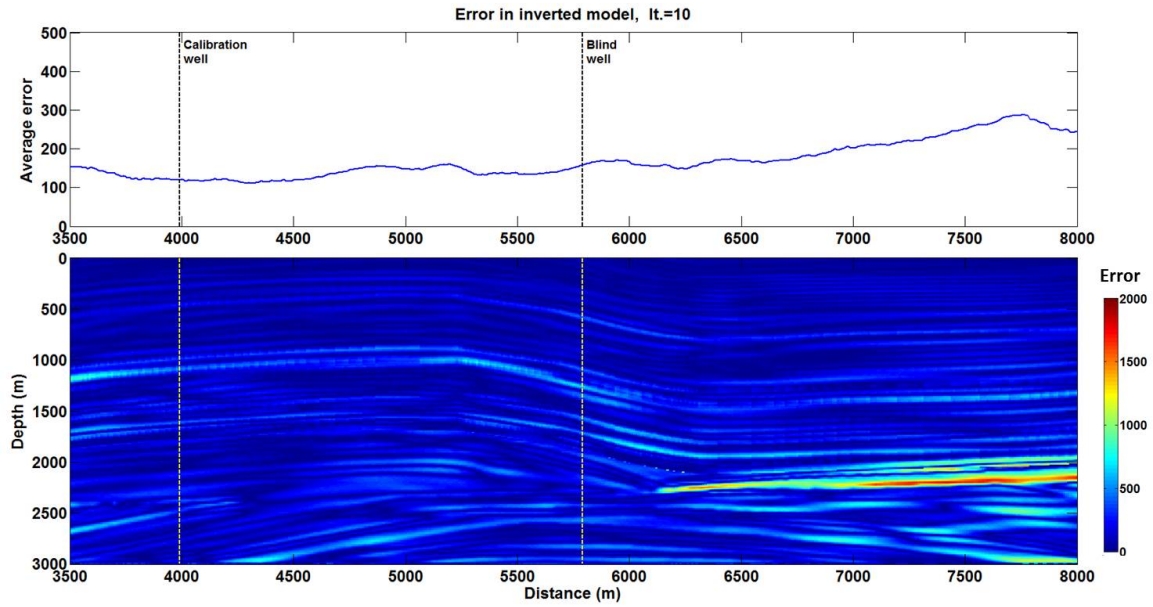
FIG. 17. Model 2: Spatial distribution of the error.

the target depth at 2500 m. The best result, outside the calibration well, is reached at iteration 5. The error steadily increases in the following iterations due to high-frequency artifacts in the shallow part.
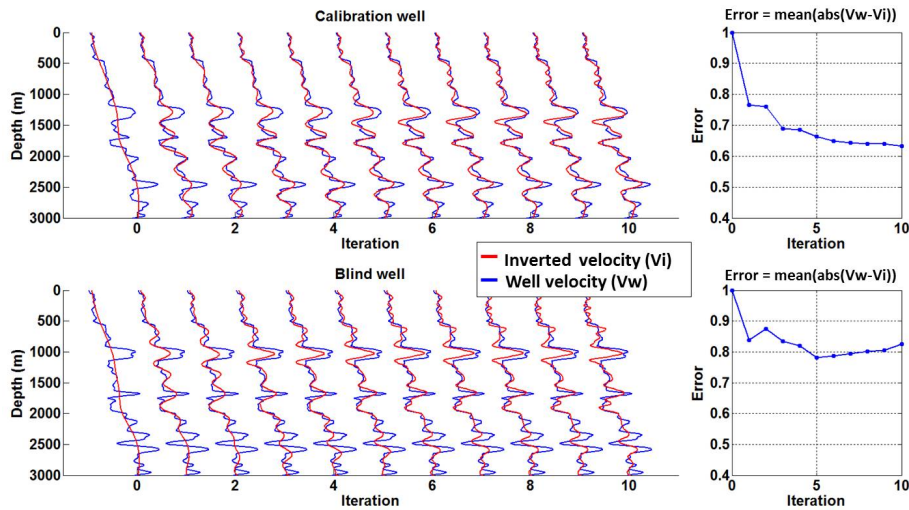

FIG. 18. Model 3: Inverted velocity evolution with iteration in calibration and blind wells.

Figure 19 shows the comparison among the initial, inverted and true models. The inverted model recovered all the main features of the true model: the faults, anticline, low-velocity target, and high-velocity body. However, the last one has not been complete defined. The horizontal bands in the shallow part are originated by the direct arrival that persists after obtaining the data residual. This means that the shallow velocity in the inverted model is significantly different than in the true model.

The spatial distribution of the error is shown in figure 17. The smallest errors occur around the calibration well as we saw for the other cases. The greatest errors are concentrated in the layers with high velocity contrasts inside the fault zone, and around the high velocity body zone. In general, the error increases as the velocity varies away the calibration well.
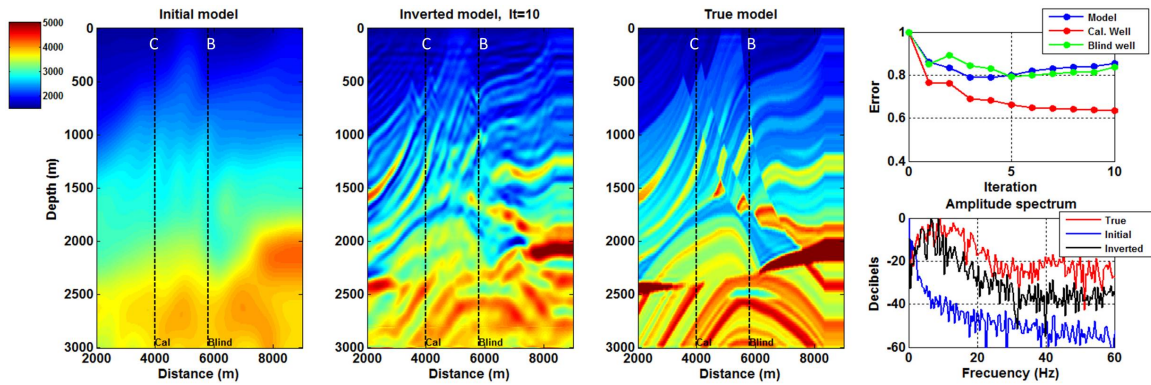

FIG. 19. Model 3: Inverted velocity evolution for the fifth iteration in calibration and blind wells.
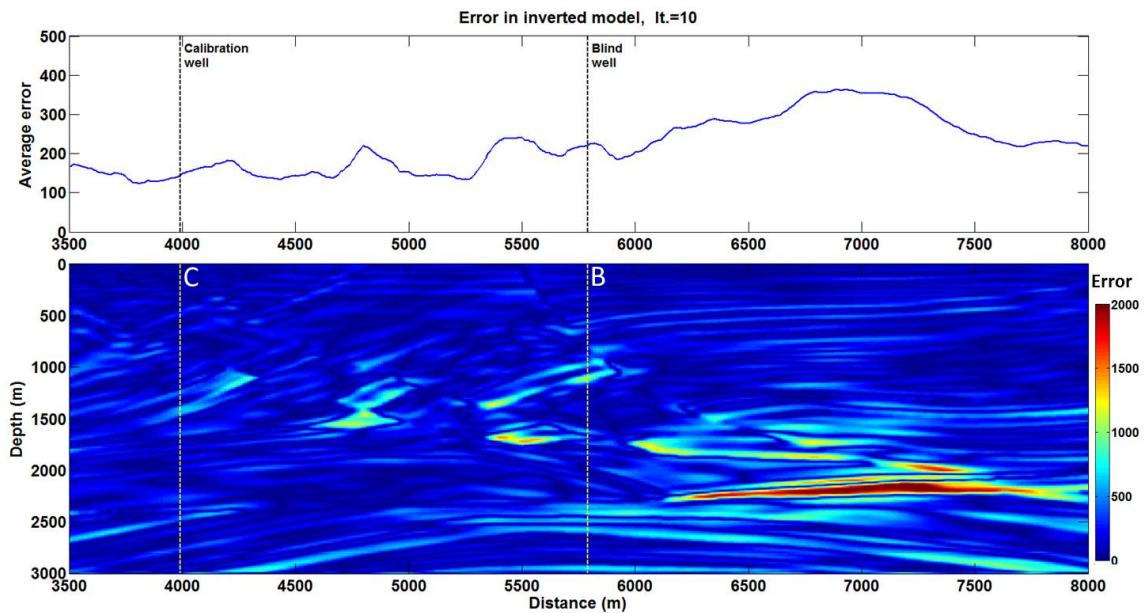

FIG. 20. Model 3: Spatial distribution of the error for the fifth iteration.

Plotting the horizontal distribution of the error for Model 1, 2 and 3 together helps to understand the role of well calibration in the context of increasing geological complexity (figure 21). We found that the error of Model 1 (flat layers) and Model 2 (modified Marmousi model with moderate lateral velocity changes) are very similar across the section except where the high velocity body is located. Here the error in model 2 steadily increases as we move into the body. There are some places where the error in model 2 is even smaller than the error in Model 1; for instance, around the calibration well. This may be happening because the Model-1 velocity has more vertical variations than Model 2 in the calibration

well location. The error of Model 3 is analogous to the error for the other models in the calibration well. The error starts to fluctuate upwards as we move away from the well and go to the faults and the high velocity body. The result of this experiment suggests that the well calibration technique provides an optimum scale for the gradient at the vicinity of the well, and produces acceptable results in the context of moderate geological complexity. However, this calibration is not optimal when strong lateral changes are present, and we may need more control wells.
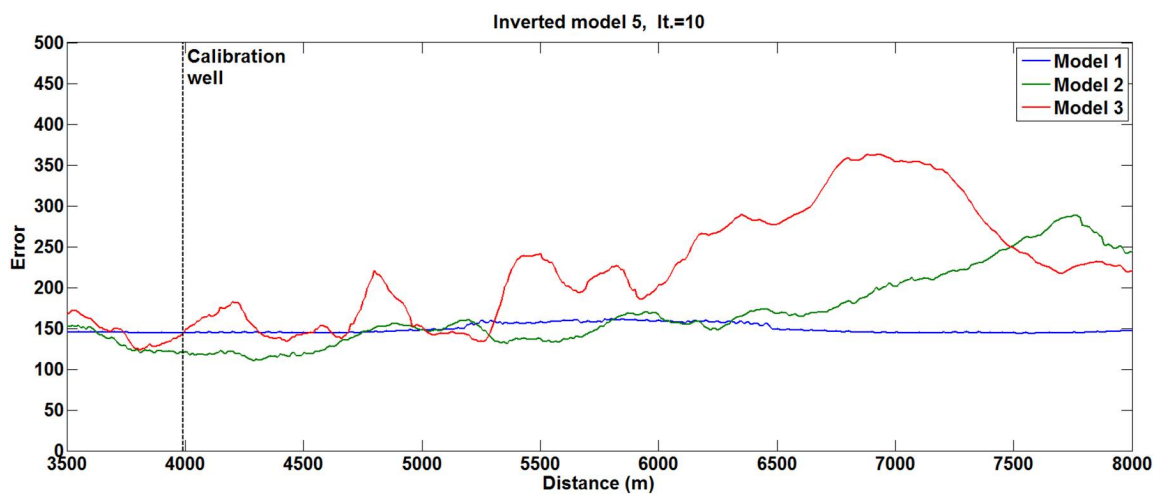

FIG. 21. Comparison of the spatial distribution error for Model 1, 2 and 3.

.

Model 3: inversion using a calibration well in each single location

An obvious thought would be that the inversion should improve if we have more calibration wells. We want to see what is the maximum improvement that this technique can provide by inverting the model under the assumption that we have a calibration well in each single model location.

Figure 22 shows the comparison of the inversion when we have only one calibration well and the hypothetical situation when we have a calibration well in each location of the model. The first thing we note is that the improvement is not as significant as we would expect; however, the high velocity body and the reservoir are better defined. The velocity in the target has a smaller error, but it is still underestimated. The variability of the scalar calculated in each location, produces continuities in the shallow layers.

Figure 23 shows the behavior of the error when we have a single calibration well and when we simulate a calibration well in each model location. The error curves are very similar in both cases, except in the zone of the high velocity body where the error effectively decreases.

Why a single well produces a similar result than the case where we have a well calibration in each location?
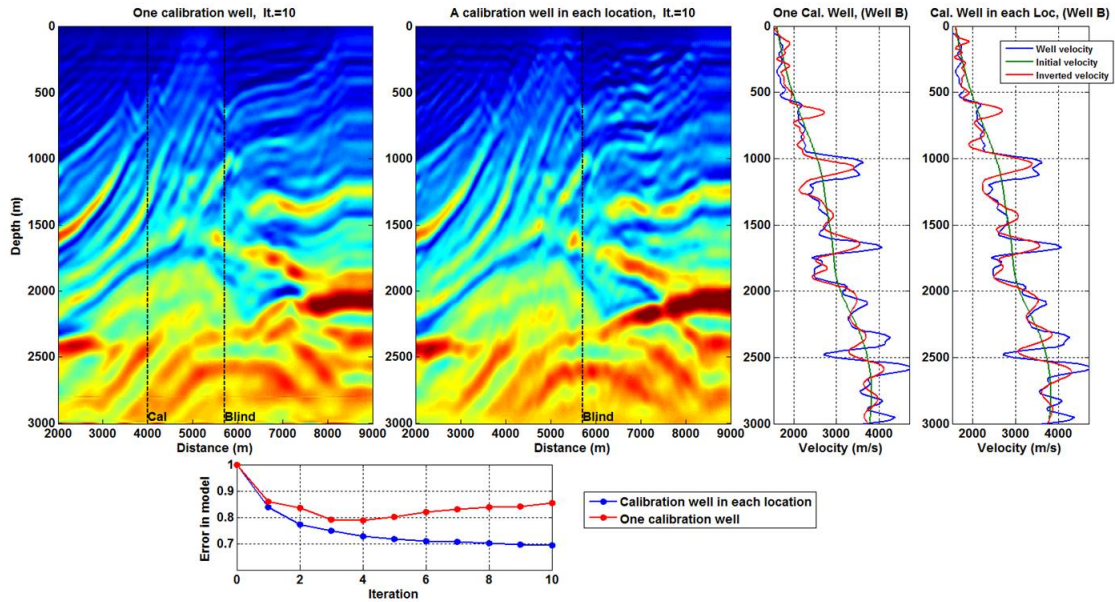
FIG. 22. Model 3: One calibration well vs calibration wells in each location.
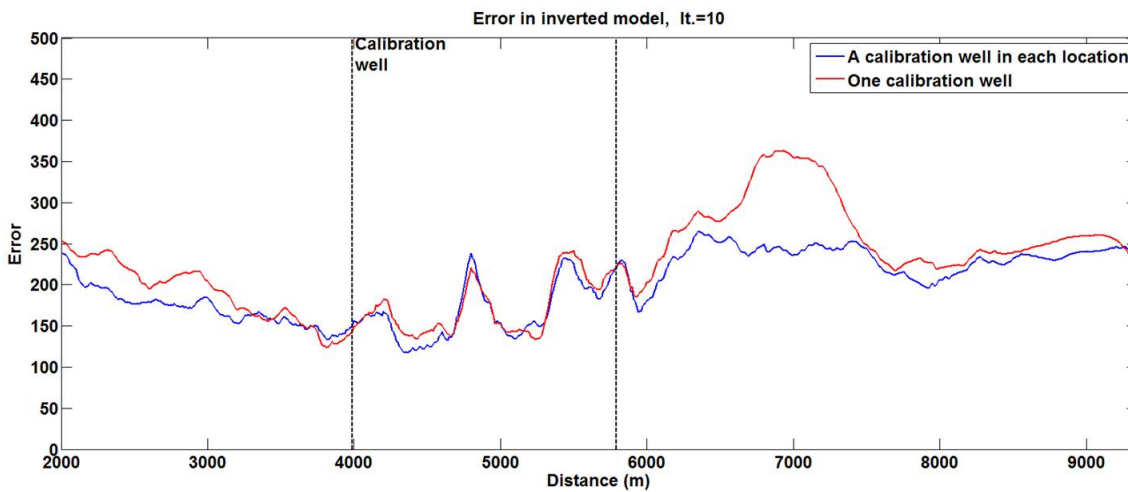
.

FIG. 23. Horizontal distribution of the error in Model 3: One calibration well vs calibration wells in each location.

We answered this question by plotting the histogram of the scales produced by using a well calibration in each location for several iterations (figure 24). When we are using the lowest frequencies, for the first iteration, the scalars are approximately uniformly distributed. As we go to higher frequencies, there are dominant scalar values that may represent zones where the geology is more similar. A single well will provide an acceptable calibration if it is close to this dominant scalar values.
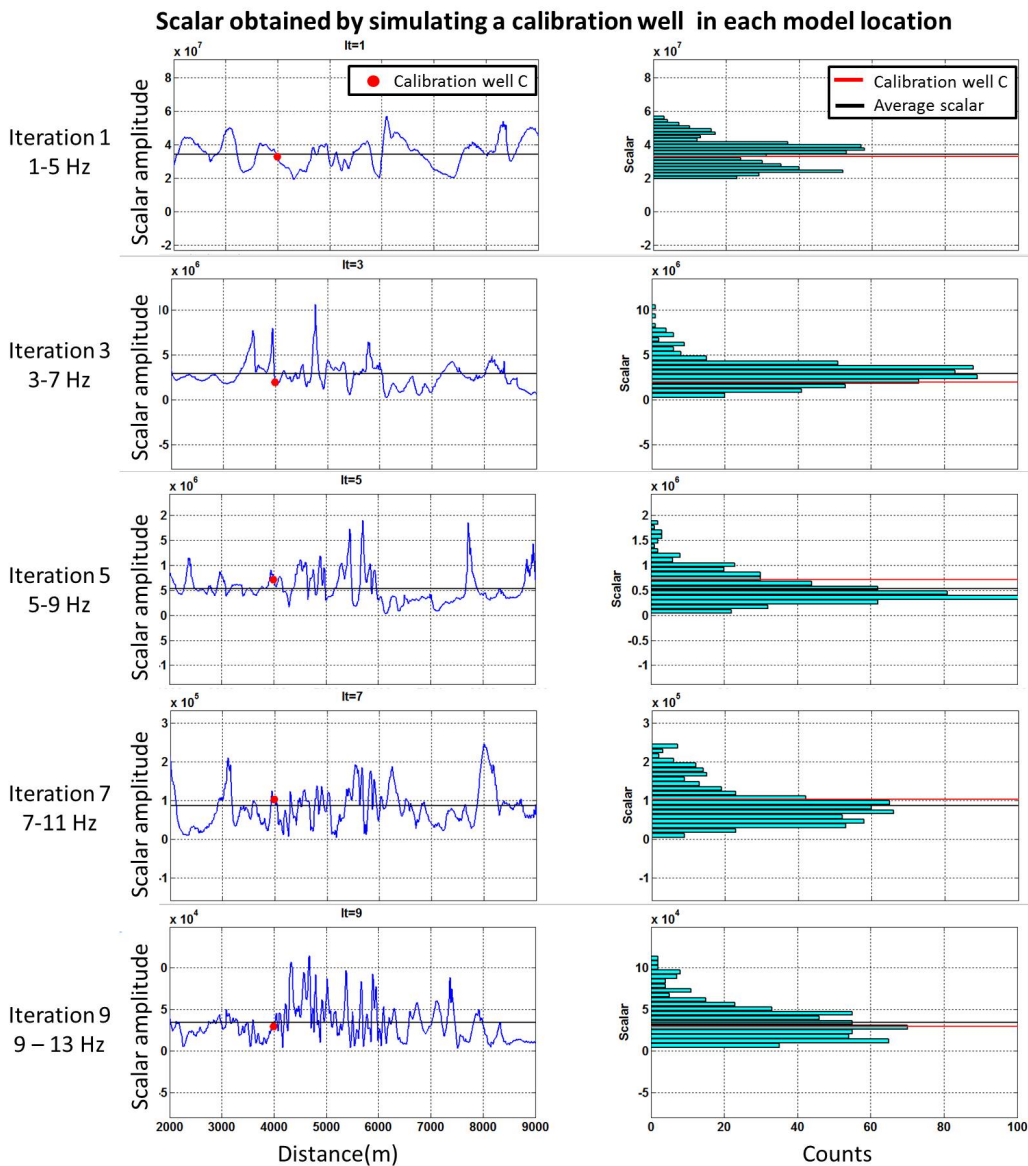
FIG. 24. Scalar variation across the section for several iterations.

CONCLUSIONS AND FUTURE WORK

The gradient, calculated with a one-way wave migration method (PSPI) under a deconvolution imaging condition, points to the correct direction to minimize the objective function in the FWI scheme. We showed that the use of well information to calibrate the gradient produces a suitable velocity perturbation to update the model. This was confirmed by the consistently low error in the well location even for the most geological complex model.

Well calibration satisfactorily performs in the presence of moderate lateral velocity changes, such as in Model 1 and 2. The error decreases each iteration as we go to higher frequencies. The inversion is able to define the target and the main geological features.

When we have strong lateral velocity variations, such as in the Marmousi Model, the inversion works properly in the shallow part, and is able to recover the main futures in the deeper part. However, the velocity tends to be underestimated as we go to deeper zones. We simulated a calibration well in each location in order to see if more wells are able to improve the inversion. However, the inversion only had a significant improvement where the high velocity body is located. We found that well calibration can be used in these settings, providing that the well is representative of the geology of the area of interest.

In future work, we will explore the option of combining the line search method and well calibration to obtain a more suitable scalar in complex geological settings. We also want to compare the one-way and two-way wave migrations in the context of high geological complexity.

The next step in our research will jump from acoustic to elastic theory. The goal will be to incorporate the knowledge and experience in AVO analysis and inversion into the FWI process following IMMI's philosophy. We will investigate how the integration of AVO analysis into the process can help to find a better scalar in mono- and multi-parameter full waveform inversion.

ACKNOWLEDGEMENTS

REFERENCES

Gazdag, J., and Sguazzero, P., 1984, Migration of seismic data by phase shift plus interpolation: Geophysics, **49**, No. 2, 124–131.

Lailly, P., 1983, The seismic inverse problem as a sequence of before stack migration: SIAM, 206–220.

Margrave, G. F., Fergurson, R. J., and Hogan, C. M., 2010, Full-waveform inversion with wave equation migration and well control: CREWES Research Report, **22**.

Margrave, G. F., Innanen, K. A., and Yedlin, M., 2012, A perspective on full-waveform inversionl: CREWES Research Report, **24**.

Pan, W., Margrave, G. F., and Innanen, K. A., 2014, Iterative modeling migration and inversion (immi): Combining full waveform inversion with standard inversion methodology: 84th Ann. Internat. Mtg., SEG, Expanded Abastracts, 938–943.

Pratt, R. G., 1999, Seismic waveform inversion in the frequency domain, part 1: Theory and verification in a physical scale model: Geophysics, **64**, No. 3, 888–901.

Shin, C., Yoon, K., Marfurt, K. J., Park, K., Yang, D., Lim, H. Y., Chung, S., and Shin, S., 2001, Efficient calculation of a partial-derivative wavefield using reciprocity for seismic imaging and inversion: Geophysics, **66**, No. 6, 1856–1863.

Tarantola, A., 1984, Inversion of seismic reflection data in the acoustic approximation: Geophysics, **49**, 1259–1266.

Virieux, A., and Operto, S., 2009, An overview of full-waveform inversion in exploration geophysics: Geophysics, **74**, 1259–1266.